Modeling of impulse waves generated by a viscous collapse in water

Quentin Kriaa,* Sylvain Viroulet,† and Laurent Lacaze‡
Institut de Mécanique des Fluides de Toulouse (IMFT), Université de Toulouse, CNRS, Toulouse, France

(Received 30 July 2021; accepted 9 March 2022; published 17 May 2022)

The generation of tsunamis by landslides has been the object of a lot of studies, focusing in particular on the wave maximum amplitude $\eta_{0,\max}$ to quantitatively assess the damage which these events may cause. The literature has long identified that this amplitude $\eta_{0,\max}$ is correlated to a Froude number $\mathrm{Fr}_{\max}$ proportional to a maximum slide front velocity $\dot{x}_{f,\max}$. Yet the dynamics of the slide needs to be determined from initial conditions to allow prediction of the maximum amplitude $\eta_{0,\max}$. Based on a canonical initial configuration, the aim of the present work is thus to better understand the transient physics connecting the landslide to the wave growth leading to the prediction of the wave maximum amplitude. In particular, the collapse of a Newtonian slide from air to water is considered here, investigating the role of two key ingredients: the slide inertia and viscous dissipation. The parameter space is systematically varied beyond laboratory and geophysical estimations to gain understanding on the fundamental process of wave formation, with two-dimensional three-phase numerical simulations using Basilisk. Results show that the column collapse of a Newtonian slide allows us to capture most of the physics of wave formation, and the correlation between $\eta_{0,\max}$ and the Froude number $\mathrm{Fr}_{\max} \propto \dot{x}_{f,\max}$ is recovered. A dynamical model of collapse reveals how the interplay between inertia and dissipation controls the slide dynamics through a Reynolds number $\mathrm{Re}(t)$ which, in turn, determines the kinematics of slide-water interface as quantified by the Froude number $\mathrm{Fr}(t)$. A simple model based on an idealised evolution of the collapse dynamics and volume conservation allows us to explicitly determine $\mathrm{Fr}_{\max}$ and $\eta_{0,\max}$ from the initial condition. This model allows us to capture results obtained from the numerical simulations and in accordance with empirical correlations usually found in the literature.

DOI: 10.1103/PhysRevFluids.7.054801

I. INTRODUCTION

The shape and dynamics of impact waves have been widely considered in the literature, particularly due to their connection with natural hazards such as tsunamis. One of the main difficulties in providing a predictive model for the characteristics of a tsunami wave is due to the variety of the triggering processes, from submarine earthquake [1] to subaerial landslides [2]. Even just in the latter situation, the possible geographical configurations leading to a tsunami are extremely diverse [3–5, for instance]. Yet, in the midst of this diversity, common features stand out from one configuration to another. That is why canonical configurations have been widely used to provide the simplest mechanisms linking the wave characteristics and the triggering process. The present work restricts to the study of subaerial landslides.

*Now at Aix Marseille Univ, CNRS, Centrale Marseille, IRPHE, Marseille, 13013, France; Corresponding author: quentin.kriaa@univ-amu.fr
†sylvain.viroulet@imft.fr
‡laurent.lacaze@imft.fr

In the specific case of subaerial landslides, the study of such canonical configurations is expected to lead to a relationship between the slide dynamics and the wave characteristics, such as its maximum amplitude $\eta_{0,max}$ and its horizontal extension. The case of a rigid slide has first been considered in the literature [6–12]. In most of these studies, a rigid block slides along an inclined plane before impacting the free surface of a water tank. With a motivation for wave prediction, the wave characteristics have been linked to several properties of the slide like its velocity, volume, and shape. More recently, the rigid block has been replaced by a granular material in order to account for more complex dynamics of the slide [13–19]. Doing so, several physical ingredients have been added to the slide which can hardly be dissociated. Among others, deformation, porosity, and compaction/dilatancy of the sliding granular medium are probably significant ones.

Several semianalytical models based on multivariable regression analyses can be found in the literature of waves induced by subaerial slides [12,19–22]. These studies identify several slide or terrain characteristics which play a role in the wave generation, group them in dimensionless numbers, and perform regressions to determine how these characteristics best correlate with measurements in the form of power laws. An example is the *impulse product parameter* [19] given by $P = \mathrm{Fr} S^{1/2} M^{1/4} \cos(6\alpha/7)^{1/2}$ with Fr a Froude number, S the dimensionless slide thickness, M the dimensionless slide mass, and α the angle of the slope where the slide is initially released. Such correlations show how each of several quantities contribute to observing a certain wave in experiments. A key aspect of this approach is therefore to identify the appropriate set of dimensionless numbers, which is usually done by dimensional analysis, or with the support of equations of motion by performing a scaling analysis [17]. Naturally, such correlations best agree with measurements. Nonetheless, the various coefficients which appear in these power laws have a physical origin whose understanding requires further modeling. The present work is precisely interested in understanding the physical grounds of the wave development.

In order to provide analytical models describing the growth of a wave, simplifications are required. In particular, for all tsunamis generated by a subaerial landslide, the Froude number has long been acknowledged as the main governing dimensionless number (see in particular Ref. [13]), with a general definition of slide-to-wave velocity ratio whose details vary between authors (e.g., Refs. [14,16,23]). Various studies evidenced accurate empirical correlations between this Froude number and wave properties such as its mechanical energy and maximum amplitude $\eta_{0,\max}$ [12,13,16,23]. Based on this observation, an analogy was built on the wave maker [24,25]. In 1970, Noda [24] established an analytical connection between $\eta_{0,\max}$ and Fr and numerically obtained that

$$\frac{\eta_{0,\max}}{H_w} = 1.32\mathrm{Fr}, \tag{1}$$

with $\mathrm{Fr} = v_p/\sqrt{gH_w}$, v_p the constant horizontal velocity of the wave maker, and H_w the initial still water level. In 1992, Goring [25] directly obtained the analytical relationship

$$\frac{\eta(t)}{H_w} = \frac{\mathrm{Fr}(t)}{1-\mathrm{Fr}(t)}, \tag{2}$$

with $\eta(t)$ the water elevation at the wave maker–water interface, $\mathrm{Fr}(t) = v_p(t)/c(t)$ with $v_p(t)$ the time-dependent piston velocity, and $c(t)$ the wave celerity at the same time. Therefore, here the piston velocity was analytically related to the wave amplitude. Note that $\eta(t)$ is maximum when $\mathrm{Fr}(t)$ is maximum itself. Recently, Sarlin *et al.* [26] showed that most of the wave types identified in their experiments of a granular column collapsing at the surface of a water tank can be produced by the motion of a piston or wave maker. For example, in the case of solitary-like waves, based on (2) and taking $c = c_{\max} = \sqrt{gH_w}[1 + \eta_{0,\max}/(2H_w)]$, the authors showed that the maximum velocity of the slide front measured in their experiments was comparable to the expected maximum wave-maker velocity $v_{p,\max}$, having

$$\frac{\eta_{0,\max}}{H_w} = \mathrm{Fr}_{\max} - 1 + \sqrt{1+\mathrm{Fr}_{\max}^2}, \tag{3}$$

with $\mathrm{Fr}_{\max} = v_{p,\max}/c_{\max}$. This highlights the robustness of the $\eta_{0,\max}(\mathrm{Fr}_{\max})$ relationship. The relationships in Ref. [26] are a first attempt to build the full dynamical process from the collapsing dynamics toward the wave generation. Nevertheless, these relationships still require the knowledge of the sliding dynamics when v_p is maximum. In other words, the wave properties are determined by measurements on the slide *after* the process of wave generation has started. Therefore, this fails at providing a full description of the multiphase system from the initial condition (slide and water at rest) until the state of wave maximum amplitude.

Overall, the studies aforementioned provide accurate laws to compute the wave maximum amplitude $\eta_{0,\max}$ only based on the Froude number. However, this Froude number, which should be proportional to the maximum slide front velocity, is usually *measured*. In order to obtain predictive models of $\eta_{0,\max}(\mathrm{Fr}_{\max})$, it would be necessary to compute the Froude number only from *initial conditions*, i.e., prior to the collapse onset. There have been some attempts (see Ref. [18]) to model similar landslide dynamics during the transient, which provide similar scalings. However, these models require numerical integrations and the use of nonlinear regression schemes to relate initial slide properties to its time-dependent characteristics during collapse.

In this framework, the present study aims at providing a model including the relevant processes for wave formation from known initial conditions. The previous discussion has shown that it requires simplifications.

According to previous results available in the literature, dominant processes can be extracted. The transient wave development is the manifestation of an energy transfer from the slide—whose interface is not initially in equilibrium with water and air because it is denser than both of them—to the pool, with some energy dissipated in the slide. The diversity of slide models which have led to a relationship $\eta_{0,\max}(\mathrm{Fr}_{\max})$ supports the idea that a granular rheology is not required to account for this energy transfer. The rate of energy transfer is expected to be governed by the slide deformation, itself controlled by the slide inertia (or density), and its dissipation (or effective viscosity). Varying both the slide inertia and dissipation modifies the slide *dynamics*. This is the starting point of this study: how do inertia and dissipation modify the slide dynamics (as quantified by a Reynolds number), and therefore the kinematics of the slide-water interface (as quantified by a Froude number) which, in turn, controls the wave maximum amplitude $\eta_{0,\max}(\mathrm{Fr}_{\max})$?

Accordingly, the present study considers the numerical modeling of an initial column collapsing into a free surface water tank, for which all the three phases (slide, water, and air above, which can be engulfed during collapse) are a Newtonian continuum. This configuration allows us to continuously vary the physical properties of the sliding phase so as to cover a wide space of the relevant dimensionless parameters and to build a predictive model of waves generated by a collapse. Although the flow may be turbulent for some waves, numerical simulations are performed in a plane since we expect two-dimensional (2D) simulations to catch the essence of the dynamics to be modelled.

The paper is organized as follows. Section II provides a description of both the physical model and the numerical method. In Sec. III, flow regimes are characterized in the parameter space. It confirms the relevance of a Newtonian rheology to both provide wave properties similar to those obtained in the experiments previously described and to recover the correlation $\eta_{0,\max}(\mathrm{Fr}_{\max})$. Subsequently, Sec. IV focuses on modeling the slide dynamics from initial conditions while Sec. V presents models to connect the slide dynamics to the transient wave growth. Together, these two sections provide predictive tools to determine the wave maximum amplitude solely from initial conditions in the configuration studied here. Conclusions are finally drawn in Sec. VI.

II. NUMERICAL MODELING OF WAVES GENERATED BY A COLUMN COLLAPSE

A. Dimensionless numbers characterizing the slumping and wave dynamics

The problem modelled in this paper is sketched in Figs. 1(a) and 1(b). It consists of an initial column of heavy fluid, referred to as the slide phase, collapsing into a pool of water, both evolving

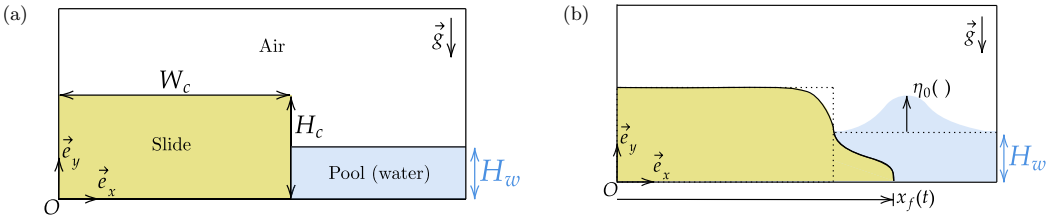

FIG. 1. Representation of the geometry of the problem (a) initially and (b) at larger times once the wave is formed and propagates.

into air. Initially, the geometry is parameterized by three lengths: the column height H_c, its width W_c, and the water depth H_w with $H_c > H_w$ for a partly immersed landslide.

Based on the slide properties which are varied in the following, two control parameters are defined:

$$R_\rho = \frac{\rho_s}{\rho_w};\ R_\mu = \frac{\mu_s}{\mu_w}, \tag{4}$$

with ρ_s and μ_s (respectively, ρ_w and μ_w) the slide (respectively, water) density and dynamic viscosity. Throughout this paper, the parameter space (R_μ, R_ρ) will thus be the main basis for comparing different simulations. As already mentioned, the geometry of the initial system is unchanged in this study, i.e., the dimensionless geometrical parameters $(W_c/H_c,\ H_c/H_w)$ are kept constant in all simulations.

Two numbers can now be defined to characterize the dynamics of the slide and wave. As previously mentioned, the wave structure and dynamics are usually related to the Froude number, defined as a slide-to-wave velocity ratio. During wave formation, the energy transfer mostly happens due to the horizontal motion of the slide pushing water when collapsing, and inducing the propagation of the wave. A temporal Froude number can therefore be defined as

$$\mathrm{Fr}(t) = \frac{u_s(t)}{u_{\mathrm{wave}}(t)} \tag{5}$$

In this equation $u_s(t) = \dot{x}_f(t)$ is the slide front velocity; therefore, this definition is intrinsically linked to the slide dynamics. In the (R_μ, R_ρ) parameter space, the slide dynamics is mostly governed by a balance between inertia and viscous dissipation, disregarding wave formation. We thus define the Reynolds number associated with the slide dynamics, and more specifically its front velocity, as

$$\mathrm{Re}(t) = \frac{\rho_s u_s(t) H_c}{\mu_s}. \tag{6}$$

It should be noted that both $\mathrm{Re}(t)$ and $\mathrm{Fr}(t)$ depend on t. A key question is thus the prediction of the relevant time to prescribe a relationship between Fr and the state of wave maximum amplitude as discussed in the literature (see Sec. I). Section III will establish the time when these two numbers should be computed to provide valuable information. For now, it shall be noted that two control parameters can be proposed from their initial estimation as

$$\mathrm{Fr}_0 = \sqrt{1 - \frac{1}{R_\rho}}\sqrt{\frac{H_c}{H_w}}, \tag{7}$$

and

$$\mathrm{Re}_0 = \frac{R_\rho}{R_\mu}\sqrt{1 - \frac{1}{R_\rho}}\frac{\rho_w}{\mu_w}\sqrt{g H_c^3}. \tag{8}$$

Compared to Eqs. (5) and (6), the characteristic velocities u_{wave} and u_s have been chosen as $u_{\text{wave}} = \sqrt{gH_w}$, the celerity of long waves, and $u_s \equiv \sqrt{(1 - 1/R_\rho)gH_c}$, the typical velocity of a parcel of density ρ_s falling in the pool over a distance H_c when subjected to buoyancy only.

Note that control parameters are therefore either (R_μ, R_ρ) or alternatively $(\text{Re}_0, \text{Fr}_0)$.

B. Numerical simulations

The three-phase DNS of air, water, and slide are performed thanks to the open-source software Basilisk [27] using a volume-of-fluid method. The latter corresponds to solving the Navier-Stokes equations for only one pseudo fluid, whose properties vary in space and time thanks to the implementation of three volume fractions $0 \leqslant f_{i\leqslant 3}(x, y, t) \leqslant 1$, one assigned to each phase. In every cell of the mesh, the local density and dynamic viscosity are implemented as an arithmetic average of the respective constant densities $\rho_{i\leqslant 3}$ and dynamic viscosities $\mu_{i\leqslant 3}$ of all phases, weighted by the volume fractions. The fluid properties therefore evolve as volume fractions are passively advected by the local velocity field. Equations are solved for an incompressible flow with finite volumes using a centered formulation of the Navier-Stokes equations (see Ref. [28]). The stability of the numerical method is ensured thanks to a CFL condition. An adaptive quadtree mesh is adopted to perform the simulation (see Ref. [29]), which adapts according to the local values of density and the velocity components (u, v) to have a sufficient resolution of their gradients. The ability of the code to capture the physics at play was initially tested with experiments from the literature, see Appendix A.

The initial geometry is sketched in Fig. 1(a). The column of slide collapses in a square domain of size L_d with a no-slip condition on the velocity field at the bottom and right wall. A symmetry condition is imposed on the left wall. This prevents the slide from wetting the left wall, as it would if a no-slip condition were imposed. At the top of the domain, the continuity of the vertical velocity component v is imposed, i.e., $\partial v/\partial y = 0$ so that air may flow in and out of this boundary. A constant pressure is also imposed at the top.

The size L_d of the square computational domain is sufficiently large compared to (H_c, W_c, H_w) to be considered irrelevant in the slide and wave dynamics throughout all simulations. The parametric study is performed with $W_c/H_c = 3.37$, $H_c/H_w = 1.95$, and $L_d/W_c = 13.8$. According to the previous discussion on the relevant parameters to characterize the influence of inertia and dissipation of the slumping phase (see Sec. II A), these geometrical parameters remain the same for all simulations.

At $t = 0$ the column is released. Then, for $t > 0$, the slide front $x_f(t)$ evolves toward increasing x while a wave is generated and propagates with an amplitude $\eta_0(t)$ at the crest of the wave, with $\eta(x, t)$ the surface elevation [see Fig. 1(b)].

In order to vary (R_μ, R_ρ), only the slide properties vary throughout this study. Therefore usual properties are adopted for water ($\rho_w = 1000$ kg m^{-3} and $\mu_w = 10^{-3}$ Pa s) and air ($\rho_{\text{air}} = 1.0$ kg m^{-3} and $\mu_{\text{air}} = 10^{-5}$ Pa s). Note that in practice landslides or cliffs collapsing in water are compressible media, hence their density is expected to vary in a wider range than usually considered for granular media in the laboratory ($\rho_s \leqslant 2000$ kg m^{-3}). Hence R_ρ is systematically varied in the wide range [1,14]. The same consequence holds for the slide viscosity so that $R_\mu \in [1, 3 \times 10^4]$. Note that this range includes the mean viscosity 8.7 Pa s (i.e., $R_\mu = 8700$) estimated from the $\mu(I)$ rheology [30,31] for a dry granular medium with the geometry hereabove.

III. FLOW CHARACTERIZATION: ADEQUACY OF A NEWTONIAN DESCRIPTION

A. Typical flow regimes in the (R_μ, R_ρ) plane

We first explore the type of waves observed in the parameter space (R_μ, R_ρ). In particular, Fig. 2 shows typical snapshots of water surface deformation and slide shape obtained in the four corners of the parameter space. The waves obtained are the ones previously reported in the literature [13,16,23,32]: solitary-like waves, hydraulic jumps, and rollers.

For $R_\mu \gg 1$ and $R_\rho \gtrsim 1$ [see Fig. 2(d) for the specific couple $(R_\mu, R_\rho) = (10^4, 1.2)$], we observe a leading wave resembling a soliton, followed by a dispersive wave train. For simplicity, this solution is referred to as a solitary-like wave in the following. In this case, the slide dynamics is expected to

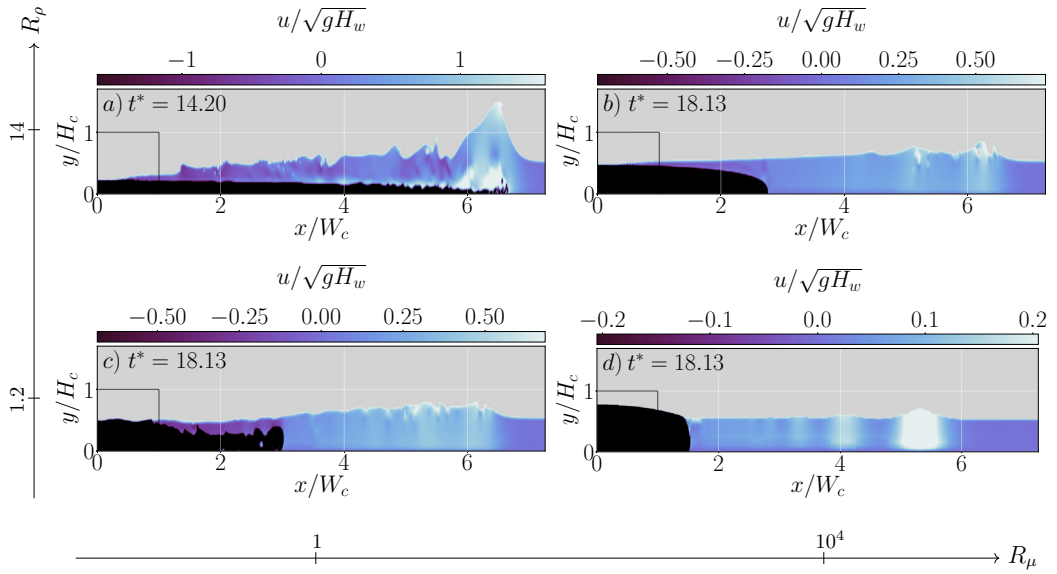

FIG. 2. Waves produced in the four extreme configurations of the parameter space. The layout (see arrows) is such that R_μ (respectively, R_ρ) increases from left to right (respectively, from bottom to top). Air and slide are respectively masked in gray and dark while the horizontal velocity field appears in water. The dimensionless time corresponds to $t^* = t\sqrt{g/H_c}$. (a) Roller $(R_\mu, R_\rho) = (1, 14)$. (b) Hydraulic jump $(R_\mu, R_\rho) = (10^4, 14)$. (c) Hydraulic jump $(R_\mu, R_\rho) = (1, 1.2)$. (d) Solitary-like wave $(R_\mu, R_\rho) = (10^4, 1.2)$. Dotted lines indicate the initial position of the slide.

be weakly inertial, as $R_\rho \gtrsim 1$, and highly dissipative, as $R_\mu \gg 1$. This induces a slow collapse of the slide with weak deformation, pushing water along the entire depth of the pool [see Fig. 2(d)]. It can be anticipated that this situation is close to a pistonlike or wave-maker-like motion inducing the wave.

Rollers, on the other hand, are obtained for a highly inertial slide, i.e., $R_\rho \gg 1$, and only slightly dissipative, i.e., $R_\mu \gtrsim 1$ [see Fig. 2(a)]. While the wave is generated, the slide deforms considerably and moves fast. The way water is set in motion is very different from the previous case. Here the slide is strongly deformed and moves fast close to its front, as if sliding underneath the wave [see the second frame of Fig. 17(b)]. Further observations show that the slide propagates rightward *with* the wave while remaining underneath, showing a long-lasting interaction between the slide and the wave. The latter eventually breaks and dissipates energy with a considerable mixing of the pool. Later, this violent wave transforms into a hydraulic jump.

Hydraulic jumps are observed in the two other corners of the parameter space, i.e., $(R_\mu \gg 1, R_\rho \gg 1)$ and $(R_\mu \gtrsim 1, R_\rho \gtrsim 1)$. An image of the configuration $(R_\mu, R_\rho) = (10^4, 14)$ can be seen in Fig. 2(b). Due to its large viscosity the slide hardly deforms. However since $R_\rho \gg 1$, the slide spreads faster than for $(R_\mu \gg 1, R_\rho \gtrsim 1)$ [Fig. 2(d)]. For $(R_\mu, R_\rho) = (1, 1.2)$, the collapse occurs on a similar timescale than the previous one, but the shape is less smooth [see Fig. 2(c)]. The slide front rolls up, as it has been observed in several experiments of impulse waves generated by a granular collapse [15]. Despite this difference, the dynamics is very similar to the previous one $(R_\mu, R_\rho) = (10^4, 14)$, leading to the same wave type.

B. Waves properties in the plane (R_μ, R_ρ)

Several types of wave have been identified in the parameter space (R_μ, R_ρ). Yet the notion of wave type has to be considered with caution since it depends on the moment when the wave is characterized. In all situations, we have observed that the collapse leads to an initial deformation

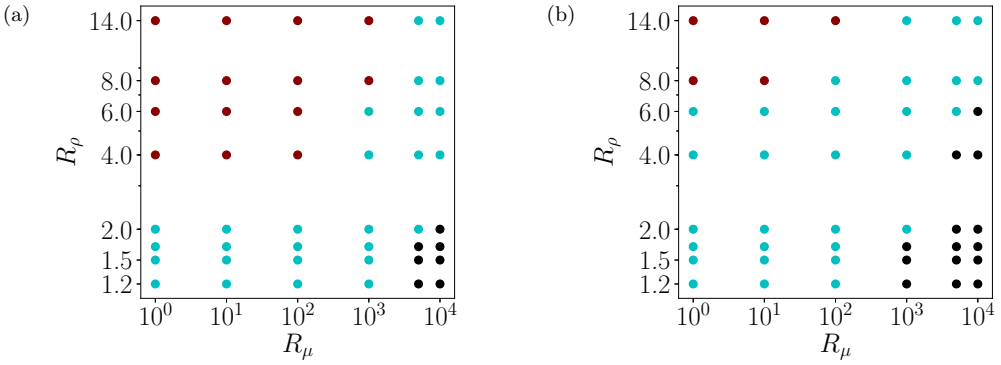

FIG. 3. Maps of the type of wave in (R_μ, R_ρ), in the close field (a) and at $x = 10W_c$ (b). Colormap: ● rollers, ● hydraulic jumps, ● solitary-like waves.

of the free surface which is nearly symmetric (as more clearly observed in the Appendix B, see Figs. 16–19). Thus, at early stages the wave type is somewhat similar in the entire parameter space. Later, the perturbation rapidly amplifies and can gently evolve into a solitary-like wave for ($R_\mu \gg 1, R_\rho \gtrsim 1$) or to an asymmetric and subsequently breaking wave otherwise (Fig. 2). In this latter case, two wave types are observed: either a roller associated with a plunging breaker or a hydraulic jump associated with a spilling breaker. Not surprisingly, on a longer timescale, both of these two types eventually lead to solitary-like waves, which stand as the solution of nonlinear water wave equations in a shallow layer limit. Consequently, when seeking the maximum amplitude of the wave, one usually distinguishes three types of wave (as in Fig. 2 for instance), while other classifications are obtained at larger timescales.

This evolution of the wave morphology in time is manifest when comparing Figs. 3(a) and 3(b), which present in (R_μ, R_ρ) the types of waves as classified previously and identified at two different locations. In these figures, wave types are distinguished with a specific color code, which is kept similar throughout the paper. Note that the gradual evolution of wave types toward solitary-like waves is confirmed: solitary-like waves gain in proportion of the parameter space at the expense of rollers, as shown in Fig. 3(b). However, the long-term evolution depends on the *early* state of the wave [i.e., Fig. 3(a)]. Thus, the prediction of wave dynamics is intimately linked to the initial phase—whatever the long-time evolution. Therefore, in the rest of this study, the "type of wave generated" refers to the classification in Fig. 3(a).

To highlight the influence of inertia and dissipation—controlled by (R_μ, R_ρ)—on the type of wave generated, the maximum wave amplitude $\eta_{0,\max}/H_w$ and the pool's maximum mechanical energy are shown in Figs. 4(a) and 4(b). Not surprisingly, Fig. 4(a) reveals that a clear correlation exists between the wave amplitude and the wave type, as rollers tend to be higher than hydraulic jumps, themselves slightly higher than solitary-like waves. Since a wave energy is connected to its amplitude, a similar correlation appears in Fig. 4(b) presenting the ratio of the maximum-to-initial mechanical energy of water, $E^{\max}_{m,w}/E_{m0,w}$ where w stands for water. These energies are computed by integrating over the whole volume of water the gravitational potential energy per unit volume ($\rho_w g y$) as well as the kinetic energy per unit volume [$\frac{1}{2}\rho_w(u^2 + v^2)$]. These last observations clearly highlight the influence of the balance between (i) the initial available potential energy associated with the slide density R_ρ and (ii) dissipation associated with the slide viscosity R_μ on the transfer of energy from the initial state to the wave. In particular, $\eta_{0,\max}/H_w$ and $E^{\max}_{m,w}/E_{m0,w}$ both increase with increasing R_ρ and decreasing R_μ.

C. Relevant dimensionless numbers of slide-to-wave interaction

To highlight the influence of the Reynolds number and the Froude number on the wave development, Fr_0 (7) and Re_0 (8) defined from the initial configuration are shown in the plane

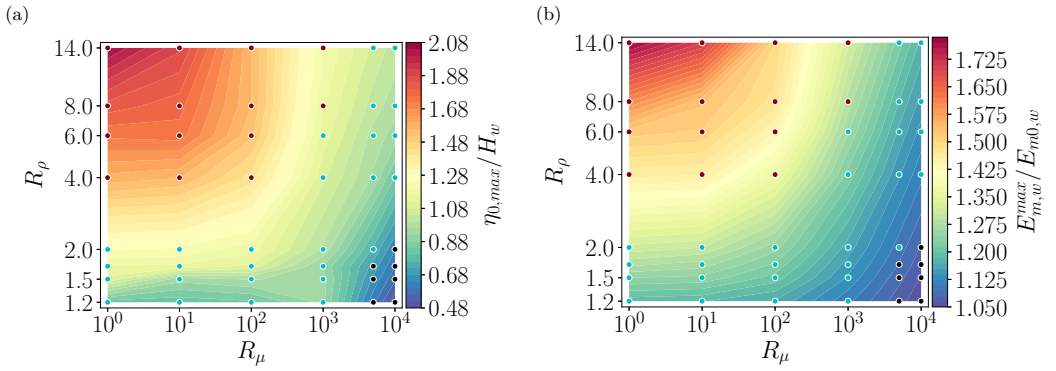

FIG. 4. (a) Map of the maximum wave amplitude. (b) Map of the maximum value reached by the pool mechanical energy throughout the whole simulation.

(R_μ, R_ρ) in Figs. 5(a) and 5(b), respectively. From (7), Fr_0 does not depend on R_μ so it can be anticipated that Fr_0 cannot account for the complete map of wave type. This is confirmed by Fig. 5(c) where no clear correlation appears between Fr_0 and the maximum wave amplitude. It implies that $u_s = \sqrt{(1 - 1/R_\rho)gH_c}$ is too coarse an approximation of the slide velocity, which requires a better estimate.

The relevant slide velocity to be incorporated in the Froude number therefore requires specific attention to define a Froude number more adequate than the control parameter Fr_0. The question

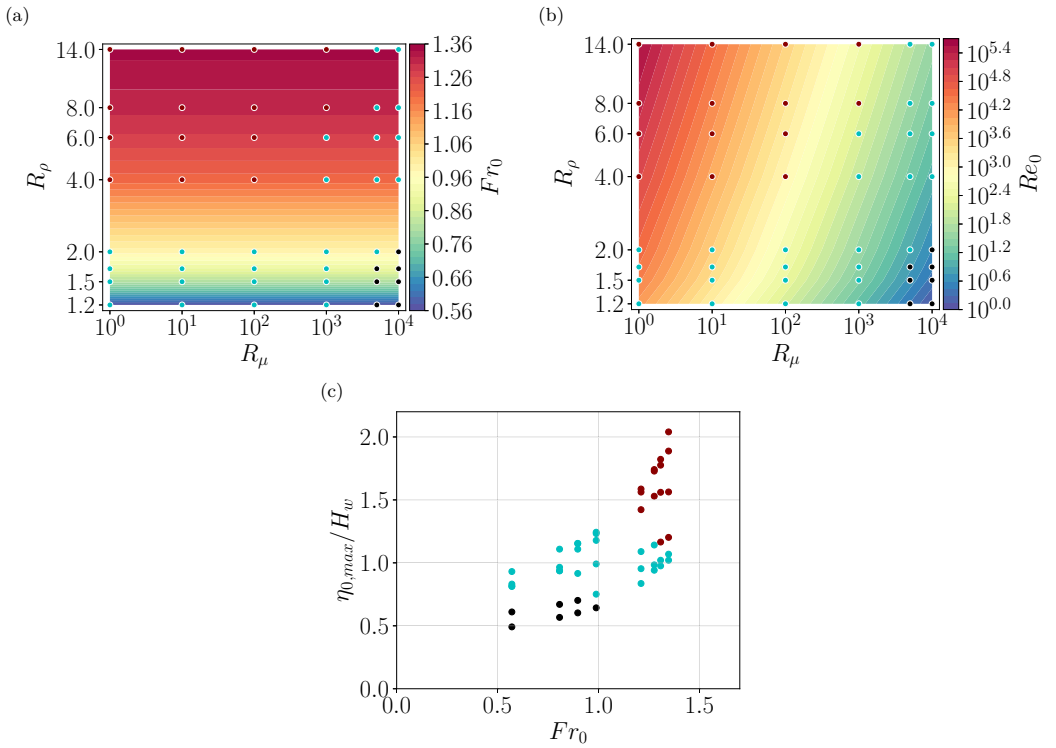

FIG. 5. Maps of (a) Fr_0 and (b) Re_0 in (R_μ, R_ρ). (c) Evolution of the maximum wave amplitude versus Fr_0.

is: When should $u_s(t)$ be computed? As long as the wave is still receiving energy from the slide, it may change shape and velocity, and therefore adapt to become a stable solitary-like wave or be disturbed and steepen until breaking. As the wave runs away from the slide, such energy transfers are expected to decrease. The wave type is thus determined when the stage of formation is over, which we refer to as the stage of "slide-wave separation." Schematically, at that moment, the wave tail is formed and runs past the slide front. It can thus be considered that separation is connected to the deceleration of the slide while the wave propagates away with a nearly constant velocity. This partly explains why, in the literature, the time of maximum slide front velocity has proved adequate to link the collapse dynamics and the state of maximum wave amplitude (see Sec. I).

From here onward, the characteristic velocity scales appearing in the definitions (5) and (6) are always taken to be $u_{\text{wave}} = \sqrt{gH_w}$ and $u_s(t) \equiv \dot{x}_f(t)$.

Now let us specifically consider the time $t_{\max}$ when the slide front velocity is maximum, as the new characteristic time to compute the Reynolds and Froude numbers: $\dot{x}_{f,\max} = \dot{x}_f(t = t_{\max})$, $\text{Re}_{\max} = \text{Re}(t = t_{\max})$, and $\text{Fr}_{\max} = \text{Fr}(t = t_{\max})$. At $t_{\max}$, Eqs. (5) and (6) read

$$\text{Fr}_{\max} = \frac{\dot{x}_{f,\max}}{\sqrt{gH_w}}, \tag{9}$$

$$\text{Re}_{\max} = \frac{R_\rho}{R_\mu}\frac{\rho_w}{\mu_w} H_c \dot{x}_{f,\max}. \tag{10}$$

For now, $\dot{x}_{f,\max}$ is determined numerically from simulations. Both $\text{Re}_{\max}$ and $\text{Fr}_{\max}$ are plotted in Fig. 6. The map of $\text{Re}_{\max}$ is very similar to that of Re_0 in Fig. 5(b) in the range of (R_μ, R_ρ) considered. As for the Froude number, a striking similarity appears between the map of $\text{Fr}_{\max}$ and the map of wave type in (R_μ, R_ρ), confirming that $t_{\max}$ is a relevant time to compute $\text{Fr}(t)$ and $\text{Re}(t)$.

The expected correlation between the Froude number $\text{Fr}_{\max}$ and the maximum wave amplitude becomes clear in Fig. 6(c). The shaded cone indicates a range of linear relations $\eta_{0,\max}/H_w = \alpha \text{Fr}_{\max}$ with α ranging in [1,1.4], as previously reported in the literature ($\alpha = 1.23$ in Ref. [23]; $\alpha = 1.32$ in Ref. [24], slightly overestimating experimental results from Ref. [33]). At larger $\text{Fr}_{\max}$, two branches of solutions are obtained in Fig. 6(c). They correspond to a bifurcation of the waves obtained for $\eta_{0,\max}/H_w \gtrapprox 1$ or almost equivalently $\text{Fr}_{\max} \gtrapprox 1$. The first branch of larger wave amplitudes is associated with $R_\mu < 10^3$, and the second branch of lower amplitudes corresponds to $R_\mu \geqslant 10^3$. The previous shaded cone is found to poorly describe these branches of solution at large $\text{Fr}_{\max}$. In this case, a power-law trend $\eta_{0,\max}/H_w = \alpha \text{Fr}_{\max}^{\beta}$ with $\beta < 1$ is revealed to be more adequate. One obtains $\beta \approx 0.74$ for the upper branch and $\beta \approx 0.45$ for the lower one. It can be noted that the power law obtained for the upper branch is close to the values reported in the literature (see Refs. [24,26] and Ref. [23] which reports a power law $\eta_{0,\max}/H_w = 1.23\text{Fr}_{\max}^{0.8}$), while the lower branch is more concave with lower values of wave amplitudes when $\text{Fr}_{\max} > 1$. To the best of the authors' knowledge, this second branch has not been reported in the literature yet. Most likely, this is because this branch corresponds to simulations with $R_\mu \geqslant 10^3$ and $R_\rho \geqslant 4$, which leads to several combinations of (R_μ, R_ρ) which can hardly be reached in experiments and are far from geophysical values.

To conclude, a Newtonian collapse contains all the required ingredients to numerically model the wave formation from a slide collapsing in water: Wave properties are similar to those obtained in experiments in the literature, and the Newtonian slide enables us to recover the correlation $\eta_{0,\max}(\text{Fr}_{\max})$. Understanding and modeling the dynamics of the slumping motion is now fundamental to predict the kinematics of the slide front, and to then make it possible to predict the wave growth by modeling the slide-wave interaction. We thus focus in Sec. IV on the analysis of the collapse dynamics to predict its front velocity from initial conditions.

IV. MODELLING THE COLLAPSE DYNAMICS

We assume in the following that three different regimes can be distinguished in the collapse dynamics.

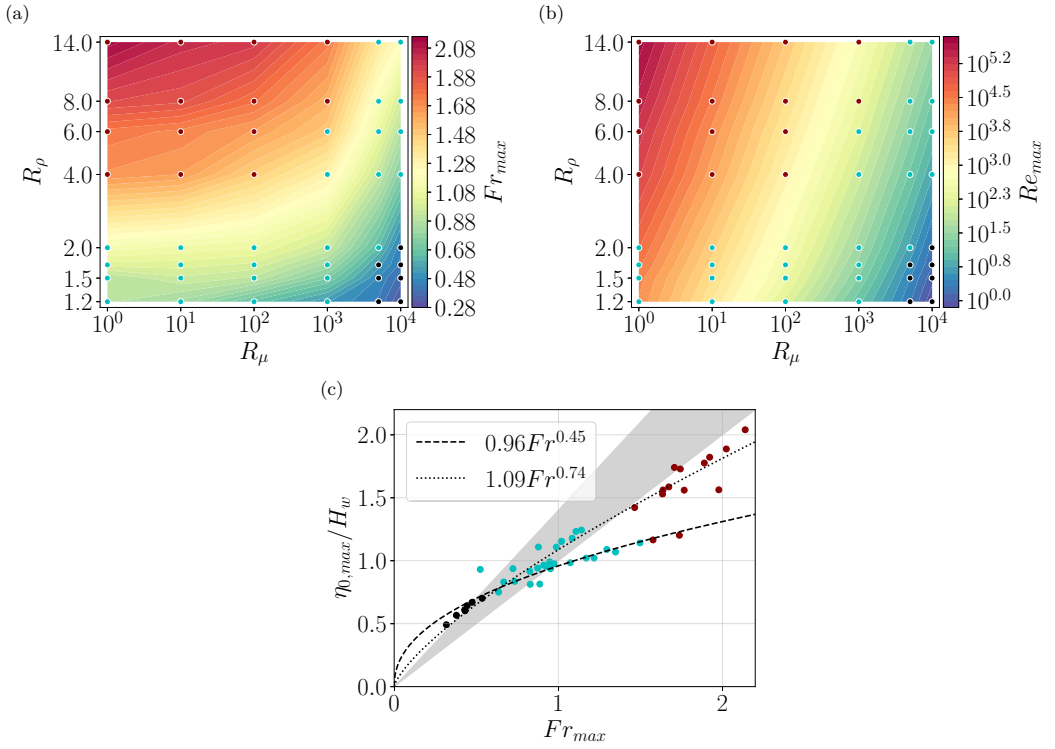

FIG. 6. Maps of $\mathrm{Fr}_{\max}$ (a) and $\mathrm{Re}_{\max}$ (b) in (R_μ, R_ρ). (c) Evolution of the maximum wave amplitude versus $\mathrm{Fr}_{\max}$. The shaded cone corresponds to slopes within the range 1–1.4. Two branches are distinguished in the region where $\eta_{0,\max}/H_w > 1$: Those having $R_\mu \geqslant 10^3$ (lower branch, dashed curve with a coefficient of correlation $r^2 = 0.884$) and those having $R_\mu < 10^3$ (upper branch, dotted curve with a coefficient of correlation $r^2 = 0.949$).

The first one is the vertical acceleration phase. As the slide freely falls under gravity, keeping a rectangular shape, conservation of mass imposes that

$$\dot{x}_{f,a} = \frac{H_c W_c g' t}{\left(H_c - \frac{1}{2} g' t^2\right)^2}, \text{ as long as } t < \sqrt{\frac{2H_c}{g'}}, \tag{11}$$

where $\dot{x}_{f,a}$ is the modelled front velocity during the acceleration phase, and $g' = g(1 - 1/R_\rho)$ is the reduced gravity.

After this initial phase, the slide may go through either an inertial regime of constant velocity or a viscous regime of deceleration [34,35]. Concerning the inertial regime, the front velocity reads (see Refs. [34] and [35] in the respective contexts of dam-breaks and gravity currents)

$$\dot{x}_{f,i} = \sqrt{g' H_c}, \tag{12}$$

where $\dot{x}_{f,i}$ stands for the front velocity in the inertial regime.

The viscous regime corresponds to a balance between viscous stress, overcoming inertia, and buoyancy. As a result the following relationship was established (see Ref. [35]):

$$\dot{x}_{f,v} = \frac{1.41}{5} \times \left[\frac{\rho_s g (R_\rho - 1)(H_c W_c)^3}{\mu_s}\right]^{1/5} t^{-4/5} \tag{13}$$

with $\dot{x}_{f,v}$ the front velocity in the viscous regime.

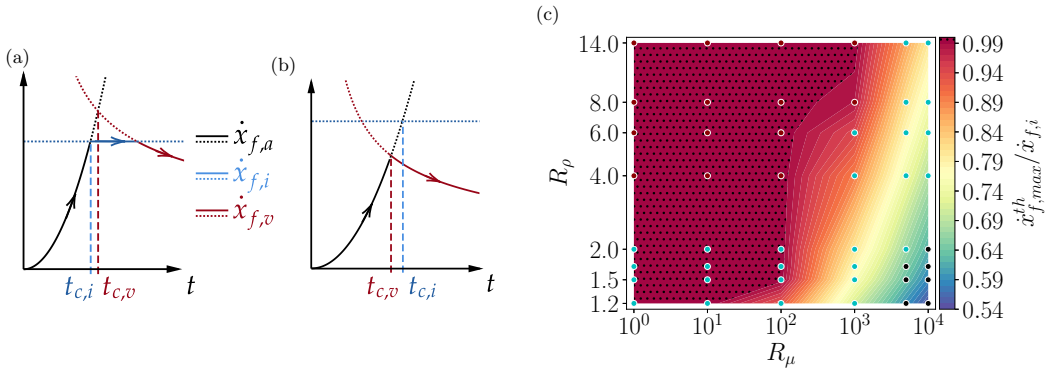

FIG. 7. Transition between regimes (a) in the order acceleration-inertial-viscous for $t_{c,i} < t_{c,v}$ and (b) in the order acceleration-viscous for $t_{c,i} > t_{c,v}$. For (a) and (b), the three regimes (11)-(12)-(13) are visible respectively in dark, blue, and red curves. The curve of every regime is solid when the slide evolves in this regime, and it is in dotted line otherwise. Vertical dashed lines indicate the intersection of the acceleration regime (in dark) with another one. (c) Theoretical value of the ratio $\dot{x}^{\text{th}}_{f,\max}/\dot{x}_{f,i}$ calculated from the analytical expressions (11)–(13). The dotted region corresponds to unit values of $\dot{x}^{\text{th}}_{f,\max}/\dot{x}_{f,i}$.

From the three regimes aforementioned, two situations can be distinguished, as sketched in Figs. 7(a) and 7(b). On one hand in Fig. 7(a), the three regimes (11)-(12)-(13) have been represented, and the dark curve of acceleration turns out to cross the inertial regime before the viscous regime. By denoting $t_{c,i}$ (respectively $t_{c,v}$) the time when the acceleration regime (11) crosses the inertial regime (12) [respectively, the viscous regime (13)], this situation corresponds to $t_{c,i} < t_{c,v}$. In that case the maximum slide front velocity is the inertial velocity $\dot{x}_{f,i}$ as modelled by (12). On the other hand, as sketched in Fig. 7(b), the acceleration phase could directly transition to the viscous regime before ever reaching the inertial regime (here the dark curve crosses the viscous regime first). In this situation, $t_{c,i} > t_{c,v}$. In that case the maximum slide front velocity is different from the constant inertial velocity $\dot{x}_{f,i}$ and is instead given by equating the velocities of Eqs. (11) and (13). Following this approach, a theoretical estimation of the maximum front velocity $\dot{x}^{\text{th}}_{f,\max}$ (where th denotes *theory*) can be obtained

$$\dot{x}^{th}_{f,max} = \begin{cases} \frac{1.41}{5} \times \left[\frac{\rho_s g(R_\rho - 1)(H_c W_c)^3}{\mu_s}\right]^{1/5} t_{c,v}^{-4/5} & \text{if } t_{c,i} > t_{c,v} \\ \sqrt{g' H_c} & \text{if } t_{c,i} < t_{c,v} \end{cases} \tag{14}$$

Note that $t_{c,i}$ and $t_{c,v}$ cannot be obtained analytically and are always computed numerically. Interestingly, the theoretical estimate $\dot{x}^{\text{th}}_{f,\max}$ enables us to distinguish two distinct groups in the (R_μ, R_ρ) plane, as shown in Fig. 7(c), where $\dot{x}^{\text{th}}_{f,\max}/\dot{x}_{f,i}$ is represented in color scale. In the inertial situation (dotted dark red region) $\dot{x}^{\text{th}}_{f,\max}/\dot{x}_{f,i} = 1$ for $t_{c,i} < t_{c,v}$, while viscous slides satisfy $\dot{x}^{\text{th}}_{f,\max}/\dot{x}_{f,i} < 1$ with $t_{c,v} < t_{c,i}$. It appears that this distinction in the (R_μ, R_ρ) plane nearly corresponds to the distinction of the two branches of solutions reported in Fig. 6(c).

It should be noted that sketches 7(a) and 7(b) are quite simplistic. The slide is expected to evidence smoother transitions from one regime to the other. Nevertheless, this approach suggests a strong correlation between the ratio $\Pi = t_{c,v}/t_{c,i}$ and the maximum slide front velocity or equivalently $\text{Re}_{\max}$ obtained from numerical results. To confirm these observations, the evolution of $\text{Re}_{\max}$ is plotted as a function of Π in Fig. 8(a) (dot symbols). This highlights the expected correlation according to numerical measurements. For a comparison, Fig. 8(a) also shows the evolution of $\text{Re}_0(\Pi)$ computed from initial conditions (red solid line). In the light of the present analysis, remember from its definition (8) that Re_0 virtually corresponds to slides which would all

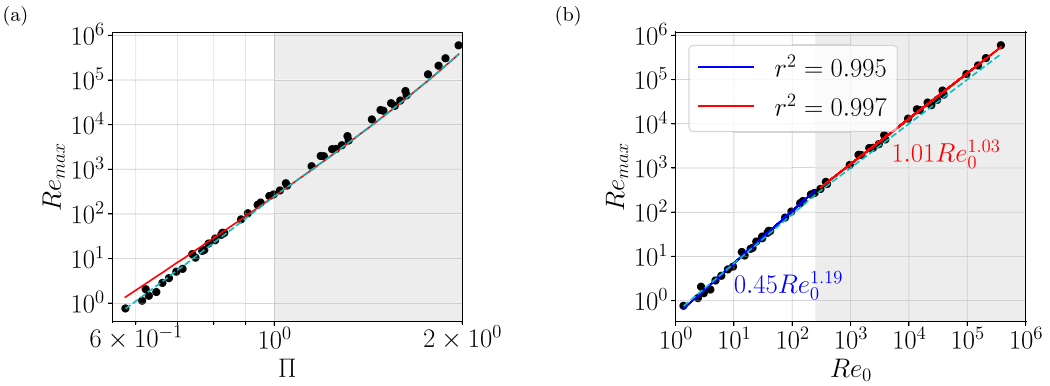

FIG. 8. (a) Correlation between the ratio $\Pi = t_{c,v}/t_{c,i}$ and the following Reynolds numbers: • measurements of $\mathrm{Re}_{\max}$, — analytical values of Re_0 from (15), - - - analytical values of $\mathrm{Re}(\dot{x}^{\mathrm{th}}_{f,\max})$ from (16). (b) Empirical regressions for $\mathrm{Re}_{\max}(\mathrm{Re}_0 < \mathrm{Re}_{0,c})$ and $\mathrm{Re}_{\max}(\mathrm{Re}_0 \geqslant \mathrm{Re}_{0,c})$, again with analytical values of $\mathrm{Re}(\dot{x}^{\mathrm{th}}_{f,\max})$ in dashed cyan line (- - -).

have an inertial maximum slide front velocity $\sqrt{g'H_c}$ [Eq. (12)]. This solution reads [see Eq. (8)]

$$\mathrm{Re}_0 = \frac{R_\rho}{R_\mu}\frac{\rho_w}{\mu_w} H_c \dot{x}_{f,i} = \frac{R_\rho}{R_\mu}\frac{\rho_w}{\mu_w} H_c \sqrt{g'H_c}, \ \forall \Pi \tag{15}$$

and is independent of R_μ [see Fig. 5(b)], which explains its noticeable inadequacy for $\Pi < 1$.

A better estimate of the Reynolds number, in cyan dashed line, is $\mathrm{Re}(\dot{x}^{\mathrm{th}}_{f,\max})$, which is obtained from Eq. (10) when replacing $\dot{x}_{f,\max}$ by $\dot{x}^{\mathrm{th}}_{f,\max}$, i.e.,

$$\mathrm{Re}(\dot{x}^{th}_{f,max}) = \frac{R_\rho}{R_\mu}\frac{\rho_w}{\mu_w} H_c \dot{x}^{th}_{f,max} = \begin{cases} \frac{R_\rho}{R_\mu}\frac{\rho_w}{\mu_w} H_c \frac{1.41}{5} \times \left[\frac{\rho_s (R_\rho - 1)(H_c W_c)^3}{\mu_s}\right]^{1/5} t_{c,v}^{-4/5} & \text{if } \Pi < 1 \\ \frac{R_\rho}{R_\mu}\frac{\rho_w}{\mu_w} H_c \sqrt{g'H_c} & \text{if } \Pi > 1 \end{cases} \tag{16}$$

For $\Pi > 1$, $\dot{x}^{\mathrm{th}}_{f,\max} = \sqrt{g'H_c}$ so solution (15) (red line) and solution (16) (cyan line) coincide. Numerical results are in good agreement with these predictions. As regards the range $\Pi < 1$, numerical results are in better agreement with model (16) than (15).

According to the previous results a correlation between the measured Reynolds number $\mathrm{Re}_{\max}$ with Re_0 is proposed in Fig. 8(b). Such a correlation with Re_0 is proposed in the framework of a *predictive* description from the *initial* state, characterized by the dimensionless number Re_0 instead of Π. Such a correlation is performed in two parts, since the previous analysis supports a distinction between the slides which are expected to cross the inertial regime ($\Pi > 1$) and those which are not ($\Pi < 1$). In terms of Re_0, this distinction is $\Pi < 1 \Leftrightarrow \mathrm{Re}_0 < \mathrm{Re}_{0,c}$ and $\Pi \geqslant 1 \Leftrightarrow \mathrm{Re}_0 \geqslant \mathrm{Re}_{0,c}$ with $\mathrm{Re}_{0,c} \simeq 248$ as suggested by Fig. 8(a). Figure 8(b) shows the obtained power laws for $\mathrm{Re}_0 < \mathrm{Re}_{0,c}$ (blue line) and $\mathrm{Re}_0 \geqslant Re_{0,c}$ (red line). For $\mathrm{Re}_0 \geqslant \mathrm{Re}_{0,c}$, the regression is very close to $\mathrm{Re}_{\max} = \mathrm{Re}_0$, although not exactly equal to it. One *cannot overlook* the subtle difference between the actual exponent 1.03 and the unit value, as would be obtained from purely theoretical prediction (16)≡(15) for $\Pi \geqslant 1$. This difference contains subtle effects of dissipation which are otherwise disregarded by the simplistic abrupt transition from acceleration regime to inertial regime as sketched in Fig. 7(a) and previously discussed. Based on these correlations, from the definitions of $\mathrm{Re}_{\max}$ and Re_0 [Eqs. (10) and (8)] we can then predict the Froude number $\mathrm{Fr}_{\max}$ as defined in (9) from initial conditions as

$$\widetilde{\mathrm{Fr}}_{\max,i\leqslant 2} = a_i Re_0^{(\alpha_i - 1)} \left[\frac{H_c(R_\rho - 1)}{H_w R_\rho}\right]^{1/2} \text{ with } \begin{cases} a_1 = 0.45, \alpha_1 = 1.19 & \text{if } \mathrm{Re}_0 < \mathrm{Re}_{0,c} \Leftrightarrow \Pi < 1 \\ a_2 = 1.01, \alpha_2 = 1.03 & \text{if } \mathrm{Re}_0 \geqslant \mathrm{Re}_{0,c} \Leftrightarrow \Pi \geqslant 1' \end{cases} \tag{17}$$

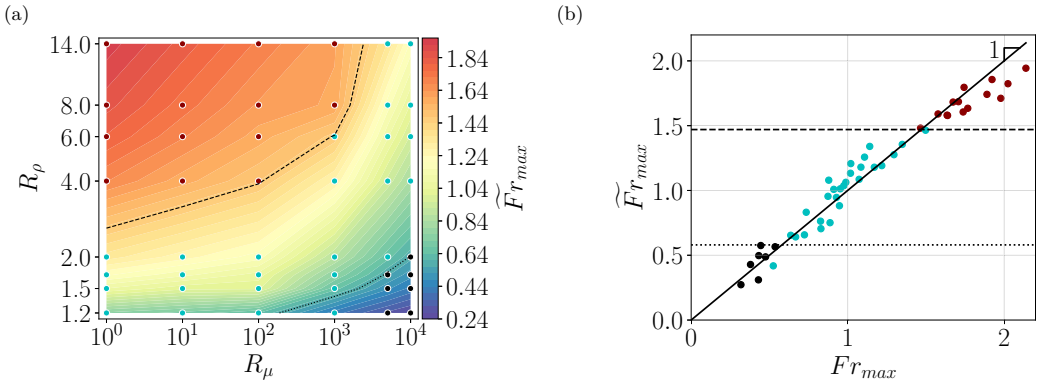

FIG. 9. (a) Map of the predicted maximum Froude number $\widetilde{\mathrm{Fr}}_{\mathrm{max}}$. (b) Comparison of $\mathrm{Fr}_{\mathrm{max}}$ and $\widetilde{\mathrm{Fr}}_{\mathrm{max}}$, respectively, the measured and predicted maximum Froude numbers. The dispersion of data around the first bisector in solid line is of 11.1%. For both figures, dots are colored as wave types and the dotted (respectively dashed) line separates hydraulic jumps from solitary-like waves (respectively, from rollers).

where the tilde over $\widetilde{\mathrm{Fr}}_{\mathrm{max}}$ stands for the predicted value of the maximum Froude number, by opposition to $\mathrm{Fr}_{\mathrm{max}}$ which is computed from numerical measurements. Note that $\widetilde{\mathrm{Fr}}_{\mathrm{max},i}$ depends on R_μ only through the term $\mathrm{Re}_0^{\alpha_i-1}$: Again, it is the difference $\alpha_i - 1 \neq 0$ in exponent which accounts for variations of the Froude number (and therefore the wave maximum amplitude) with R_μ in the parameter space. The predicted Froude number $\widetilde{\mathrm{Fr}}_{\mathrm{max}}$ (the index $i \leqslant 2$ is omitted from here on) is shown in the parameter space (R_μ, R_ρ) in Fig. 9(a). A clear similarity appears with the map of $\mathrm{Fr}_{\mathrm{max}}$ in Fig. 6(a). The two quantities $\mathrm{Fr}_{\mathrm{max}}$ and $\widetilde{\mathrm{Fr}}_{\mathrm{max}}$ are compared quantitatively in Fig. 9(b) where data points scatter around the first bisector with a dispersion of 11.1%. Such a value is low enough to enable the prediction of the Froude number with Eq. (17). Figures 9(a) and 9(b) also show that $\widetilde{\mathrm{Fr}}_{\mathrm{max}}$ is an efficient predictor of the type of wave generated with $\widetilde{\mathrm{Fr}}_{\mathrm{max}} \leqslant 0.58$ corresponding to solitary-like waves and $\widetilde{\mathrm{Fr}}_{\mathrm{max}} \geqslant 1.47$ corresponding to rollers. Note that these thresholds are only indicative as the transition from one wave type to the other is smooth in (R_μ, R_ρ), making the discrimination between wave types somewhat uncertain close to these two thresholds. Finally, note that the expression of $\widetilde{\mathrm{Fr}}_{\mathrm{max}}$ shows no dependency on W_c, even though it is expected to influence the maximum slide front velocity according to Eqs. (11) and (13). Its influence is implicitly hidden in the regression coefficients a_i and α_i of Eq. (17).

V. MODELLING THE WAVE FORMATION

A. Geometrically based models

The aim of this section is to propose simple models for the generation of the wave according to the slumping motion as described previously. Such modeling is obviously a challenging task if one considers the entire complexity of such a system. We propose here to adopt a simple argument of volume conservation as the basis of the model, as sketched in Fig. 10. In particular, one considers that during a short time dt, the volume per unit width dA_r of water *rising* above the still water level is equal to the volume per unit width dA_m of water *moved* by the amount of slide going underneath the still water level. Thus, we get:

$$dA_m(t) = dA_r(t). \tag{18}$$

Based on this volume conservation, several assumptions are proposed to simplify the time evolution of the geometry and of the coupled dynamics of this complex system. This will enable us

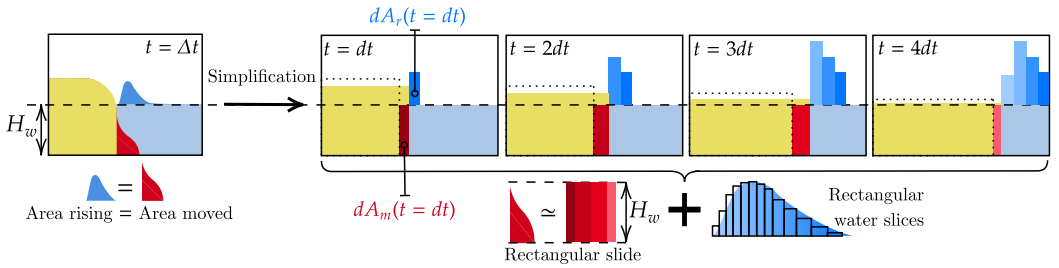

FIG. 10. The morphologies of the slide and wave during formation are simplified based on hypotheses (H1)–(H6), and the result is illustrated at successive timesteps. Dotted lines always indicate the position of the slide interface at the previous timestep. The dashed line shows the initial depth of still water. Between consecutive timesteps water displaced appears in red and water rising in blue. Proportions are not respected in order for red and blue areas to all be visible.

to propose a connection between the slide front motion and the water elevation. For this purpose, we first discuss assumptions to model dA_m and then dA_r.

Our first hypothesis is that water is only displaced because some volume of slide dA_m goes underwater, displacing an equal amount of water dA_m (H1). This means that once the slide is entirely underwater, its motion has no influence on the wave growth because pressure effects are neglected here. Then, at all times, the slide is assumed to displace water as long as it moves below the initial still water level H_w (H2).

Now, the specific case of our first geometrically based model is sketched in Fig. 10. Here the slide is assumed to remain rectangular during the whole dynamics of collapse as suggested by Fig. 2(d) at large R_μ and low R_ρ (H3). This allows us to simply connect the area displaced by the slide and the front displacement $dx_f(t)$: From (H1)–(H3), it appears that the slide front displaces a volume $dx_f(t)H_w$ during dt. As a consequence of (H1), the slide can move water only when its height is above H_w. Later, no extra volume of slide is injected underneath H_w (see Fig. 10) so that the slide deforms underwater with no contribution to the water rise. Since the slide area is constant and equal to H_cW_c, wave formation stops when $x_f(t_{\text{end}}) = W_cH_c/H_w$. Therefore, as long as $x_f \leqslant W_cH_c/H_w$, we obtain

$$dA_m(t) = dx_f(t)H_w. \tag{19}$$

As sketched in Fig. 10, a volume of water rises due to the slide motion during dt. In order to predict this water elevation, we assume that during dt the water level rises with an elevation $\eta^f(t)$ over a length $dl(t)$ (H4). This water column is assumed to be located at the slide front (H5), hence the notation f in exponent. Assumptions (H4) and (H5) imply $\eta^f(t) = \eta[x_f(t) \leqslant x \leqslant x_f(t) + dl(t)]$. Finally, the width $dl(t)$ is assumed to result from the velocity difference between water perturbations (celerity c) and the slide front (velocity $\dot{x}_f$) so that $dl(t) = c(t)dt - \dot{x}_f(t)dt$ (H6). As a consequence of this assumption, this model is relevant only as long as the slide front is slower than water waves, i.e., $\text{Fr}(t) \leqslant 1$. Considering the celerity of perturbations to be that of gravity waves in the shallow layer limit $c(t) = \sqrt{gH_w}$, assumptions (H4)–(H6) lead to

$$dA_r(t) = \eta^f(t)[\sqrt{gH_w} - \dot{x}_f(t)]dt. \tag{20}$$

In the limit $dt \to 0$, Eq. (18) then leads to

$$\dot{x}_f(t)H_w = \eta^f(t)[\sqrt{gH_w} - \dot{x}_f(t)] \iff \text{Fr}(t) = \frac{\eta^f(t)/H_w}{1 + \eta^f(t)/H_w} \tag{21}$$

as long as $x_f \leqslant W_cH_c/H_w$ and $\text{Fr}(t) \leqslant 1$. By contrast, the celerity of perturbations may depend on the wave amplitude as for solitary-like waves $c(t) = \sqrt{g[H_w + \eta^f(t)]}$. Proceeding similarly, one is

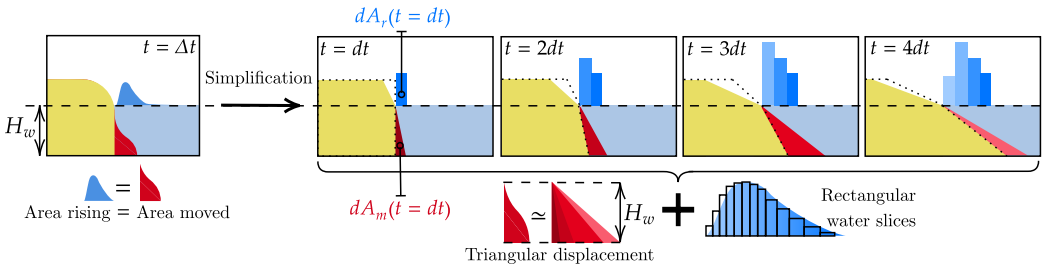

FIG. 11. The morphologies of the slide and wave during formation are simplified based on hypotheses (H3b)–(H6b), and the result is illustrated at successive timesteps, with the same system of symbols as in Fig. 10.

led to the relationship

$$\mathrm{Fr}(t) = \frac{\eta^f(t)/H_w}{\sqrt{1+\eta^f(t)/H_w}}. \tag{22}$$

Let us now turn to a second model, based on observations of wave formation at large Froude numbers, see in particular Figs. 2(a), 2(b), and 2(c). In this case, the slide front is assumed to deform as a triangle of decreasing slope with increasing time, keeping the triple point $(x, y) = (W_c, H_w)$ fixed in time (H3b) as illustrated in Fig. 11. Keeping assumptions (H1) and (H2), the surface area displaced underneath H_w, $dA_m(t)$, is mostly unmodified (disregarding a $1/2$ coefficient).

Concerning the rising water area $dA_r(t)$, water is still assumed to rise as successive columns of width $dl(t)$ and elevation $\eta^{tp}(t)$ (H4b). However, these columns are now assumed to form right in front of the supposedly fixed triple point $(x, y) = (W_c, H_c)$ (H5b), hence the notation $\eta^{tp}(t) = \eta[W_c \leqslant x \leqslant W_c + dl(t)]$. Water columns then develop above a varying water depth (as sketched in Fig. 11). The sixth assumption is modified in that the slide front velocity does not need to be subtracted since perturbations propagate away from the *fixed* triple point: $dl(t) = c(t)dt$ (H6b). Again, two cases can be considered to model the celerity $c(t)$. For intermediate Froude numbers (see Figs. 18 and 19) waves propagate above the triangular-like slide. Perturbations appear just in front of the triple point at $x \simeq W_c$ where the water depth is infinitesimal as $dl(t)$. Hence their celerity is assumed to depend only on their elevation under the form $c(t) = \sqrt{g\eta^{tp}(t)}$ so that

$$\mathrm{Fr}(t) = \left[\frac{\eta^{tp}(t)}{H_w}\right]^{3/2}. \tag{23}$$

For the largest Froude numbers, the slide deforms to such an extent that perturbations quickly develop over a depth of order H_w (see Fig. 17). Consequently the celerity $c(t) = \sqrt{gH_w}$ is adopted, leading to

$$\mathrm{Fr}(t) = \frac{\eta^{tp}(t)}{H_w}. \tag{24}$$

Equations (23) and (24) hold as long as the receding top of the slide has not reached the left wall at $x = 0$, which yields $x_f(t) \leqslant W_c(H_c/H_w - 1)$. In fact, when the front travels a distance $dx_f(t)$, due to volume conservation the slide top recedes a distance $dl(t) = dx_f(t)H_w/(H_c - H_w)$ (see Fig. 11). After integration, imposing $l(t) \leqslant W_c$ leads to the previous condition.

The two models of rectangular and triangular collapse are consistent with previous observations [23,32], and clarify the link between the slide horizontal motion and the wave formation as anticipated in Sec. III C. The Froude number $\mathrm{Fr} \propto \dot{x}_f$ quantifies the volume flux of water per unit depth (and time and width) displaced by the slide, which must rise above H_w. In particular, we note the absence of any correlation between the amplitude $\eta_{0,\max}/H_w$ and the ratio $R_\rho \mathrm{Fr}^2_{\max}$ which would

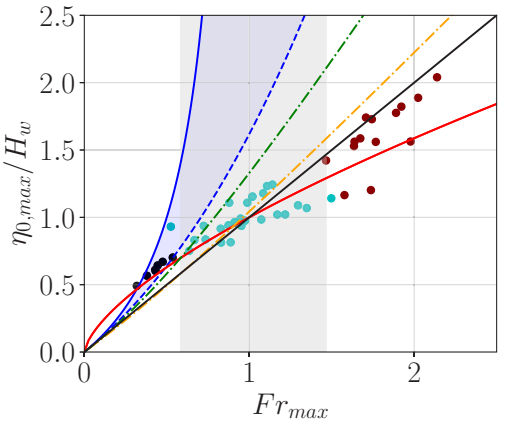

FIG. 12. Comparison of models of wave formation to numerical measurements, at the specific moment $t_{\max}$ when the slide front velocity is maximum. Dimensionless wave amplitudes are shown as a function of the measured Froude number $\mathrm{Fr}_{\max}$. Bullet points: measurements of $\eta_{0,\max}/H_w$. Rectangular collapse: —— Eq. (25), - - - Eq. (26). Triangular collapse: —— Eq. (24), —— Eq. (27). Dash-dotted lines correspond to the models from Sarlin *et al.* [26] for a solitary-like wave (-.-.-.) and a bore (-..-..). The shaded Froude numbers correspond to the region of hydraulic jumps identified in Fig. 9.

quantify a momentum flux, as found in analyses based on momentum transfer from the slide to the wave, see Ref. [36]. As for the exact relationship between $\mathrm{Fr}(t)$ and $\eta^f(t)$ or $\eta^{tp}(t)$ it combines two elements: volume conservation and, during dt, depending on Eqs. (21)–(24), the relative ability of the wave to store water vertically through $\eta^f(t)$ or $\eta^{tp}(t)$ for a slower wave, or horizontally through $dl(t)$ for a faster wave.

B. Implications for wave prediction

Models of Eqs. (21)–(24) are now tested. Equation (24) does not need to be inverted. As for Eqs. (21)–(23), they respectively lead to Eqs. (25)–(27) as follows:

$$\frac{\eta^f(t)}{H_w} = \frac{\mathrm{Fr}(t)}{1-\mathrm{Fr}(t)}, \tag{25}$$

$$\frac{\eta^f(t)}{H_w} = \frac{\mathrm{Fr}^2(t)}{2}\left[1+\sqrt{1+\frac{4}{\mathrm{Fr}^2(t)}}\right], \tag{26}$$

$$\frac{\eta^{tp}(t)}{H_w} = \mathrm{Fr}^{2/3}(t). \tag{27}$$

The dimensionless wave maximum amplitude is deduced from Eqs. (24) and (25)–(27), and shown in Fig. 12 along with numerical measurements. In the framework of the rectangular model, the actual dependency of the wave maximum amplitude with $\mathrm{Fr}_{\max}$ is expected to lie in the blue shaded region (see Fig. 12) defined by Eqs. (25) and (26) which can be considered as two end-members for the dependency of the celerity of perturbations with their own elevation. Recall that the model of rectangular collapse is expected to hold for slides which hardly deform, typically leading to solitary-like waves for $\mathrm{Fr}_{\max} \leqslant 0.58$ (see Fig. 9). The dark dots associated to these waves are nicely delimited by Eqs. (25) and (26), they appear to lie within the blue shaded region up to $\mathrm{Fr}_{\max} = 0.58$.

As expected, the triangular model of Eqs. (24) and (27) better catches the state of maximum wave amplitude of hydraulic jumps and breaking waves. The uppermost branch of amplitudes is best

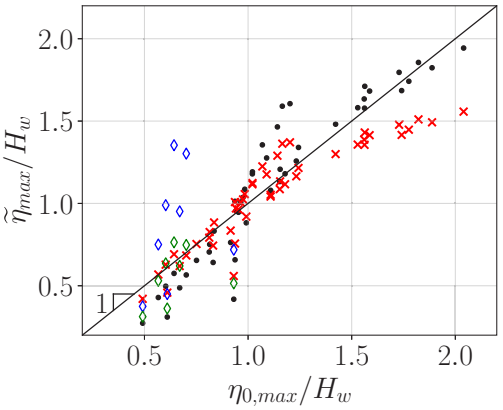

FIG. 13. Assessment of the capacity of previous equations (in ordinate) to predict $\eta_{0,\max}/H_w$ from initial conditions. Rectangular collapse: ◇ Eq. (25), ◇ Eq. (26). Triangular collapse: ● Eq. (24), × Eq. (27).

caught by Eq. (24), while the lowermost branch is best caught by Eq. (27). This is consistent with the uppermost branch corresponding to viscosity ratios lower than 10^3 (see end of Sec. III C) for which slides considerably deform, hence waves mostly evolve over a constant depth H_w. On the opposite, the lower branch corresponds to larger viscosity ratios $R_\mu \geqslant 10^3$ whose slides slightly deform, hence the celerity of perturbations mostly depends on their elevation, irrespective of the negligible underlying water depth. This dichotomy between Eqs. (24)–(27) and the two branches of solutions only holds where data points are separated, i.e., for $\mathrm{Fr}_{\max} \geqslant 1$. For $\mathrm{Fr}_{\max} \leqslant 1$, Eq. (27) best captures all numerical measurements. This is consistent with low Froude numbers $\mathrm{Fr}_{\max}$ corresponding to slides of little deformation. Additionally, numerical simulations show that the lower $\mathrm{Fr}_{\max}$, the earlier the moment when $\mathrm{Fr}_{\max}$ is reached, the less time for the slide to deform and the closer the whole wave to the triple point, hence the thicker the slide underneath the wave, the more valid Eq. (27). As $\mathrm{Fr}_{\max}$ increases above unity, depending on the slide deformability, waves end up on either of the two branches of solutions.

Compared to preexisting models from Ref. [26] (see the green and orange dash-dotted lines in Fig. 12), the present model of rectangular slide shows a slight improvement for $\mathrm{Fr}_{\max} \leqslant 0.58$, while the model of triangular slide shows a noticeable improvement. The linear trend of Eq. (24) is closer to the uppermost branch which is sublinear for $\mathrm{Fr}_{\max} > 1$, and the concavity of measurements (especially on the lowermost branch) is nicely captured by Eq. (27). Note that the concavity of Eq. (27) remains slightly insufficient for the lowermost branch at $\mathrm{Fr}_{\max} \geqslant 1$. Lower ordinates suggest waves propagating faster for a given $\mathrm{Fr}_{\max}$. This may be captured by accounting for the contribution of a nonnegligible water depth γH_w ($0 < \gamma < 1$) to the celerity of perturbations.

The contrast between preexisting models and the ones presented here can be explained by the fact that for most waves, the wave maximum amplitude is reached before wave types can be identified [i.e., before hydraulic jumps and breaking waves reach their quasisteady state which defines their wave type in Fig. 3(a), see Sec. III B]. Hence, equations established for steady solitons and steady bores broadly capture the waves characteristics (as evidenced by the green and orange curves from Ref. [26]), but their accuracy at $t_{\max}$ is inevitably limited.

We now directly assess the predictive capacity of Eqs. (24)–(27). To do so, we evaluate the maximum wave amplitude from these equations, obtained at $t_{\max}$ when the slide front velocity is maximum, and use the Froude number $\widetilde{\mathrm{Fr}}_{\max}$ predicted from (17). Note the difference of notations: The amplitude $\eta_{0,\max}$ has no exponent since it is measured, while amplitudes from Eqs. (24)–(27) have an exponent indicating where the wave is assumed to appear (at the slide front f or at the triple point tp), and additionally have a tilde when computed from the *predicted* maximum Froude

number $\widetilde{\mathrm{Fr}}_{\max}$ to indicate the predictive nature of these amplitudes. Therefore, $\widetilde{\eta}^{f}_{\max}$ and $\widetilde{\eta}^{tp}_{\max}$ are only computed from the initial state and not from the unknown dynamics of the slide as usually done in the literature.

Predicted amplitudes are directly compared to the measured value $\eta_{0,\max}/H_w$ in Fig. 13. Equations (25) and (26) for a rectangular collapse are only compared in the range $\mathrm{Fr}_{\max} \leqslant 0.58$, and lead to respective overall errors of 32.8% and 16.7% compared to numerical measurements. As for Eqs. (24) and (27) for triangular collapses, they respectively lead to overall errors of 15.3% and 17.0% considering all data points. Hence, Eqs. (26), (24), and (27) prove to satisfactorily predict the wave maximum amplitude knowing that the relative difference between $\mathrm{Fr}_{\max}$ and $\widetilde{\mathrm{Fr}}_{\max}$ already amounts to 11.1%, as previously assessed from Fig. 9(b).

VI. CONCLUSION

The three-phase numerical simulations performed in this work show that the physics of wave formation is captured by the simplified model of a Newtonian column collapsing in water. The interplay between two parameters, the slide inertia and viscous dissipation, proves decisive in the formation of a certain type of wave among three (Fig. 3). For dense columns of low viscosity, inertia predominates over viscous dissipation leading to a violent collapse and the formation of rollers. On the opposite, slides of low inertia and large viscosity hardly deform and smoothly generate solitary-like waves. Intermediate situations lead to hydraulic jumps, breaking only close to the water free surface. Hydraulic jumps have been observed to divide in two subcategories which appear as two branches in Figs. 6(c) and 12. To the best of the authors' knowledge, one branch has gone unobserved in experiments or field studies. This may be explained by the fact that corresponding values of (R_μ, R_ρ) cannot be reached in either context.

An analytical model describes the slide evolution as a succession of transitions between typical dynamical regimes. It shows how the balance between inertial and viscous effects through a Reynolds number $\mathrm{Re}(t)$ [Eq. (6)], controls the transient front motion, and consequently the kinematics of the slide-water interface as quantified by a Froude number $\mathrm{Fr}(t)$ [Eq. (5)]. After a regression on numerical measurements, the maximum value $\mathrm{Re}_{\max}$ [Eq. (10)] of the Reynolds number is calculated from initial conditions only. This enables us to compute the maximum Froude number $\widetilde{\mathrm{Fr}}_{\max}$ [Eq. (9)] directly from initial conditions, and to anticipate the type of wave generated, should the slide collapse. Further modeling is required to compute $\mathrm{Re}_{\max}$ with no regression. Additionally, beyond the state of maximum Reynolds and Froude numbers, a better understanding and modeling of the transitions between regimes of collapse would ideally enable to connect the initial state to the whole transient collapse dynamics.

To connect this dynamics to the transient wave growth, analytical models of wave formation are developed, based on volume conservation. As the slide displaces some water, an equal volume of water rises as a hydrodynamic perturbation which travels with a velocity depending on its finite amplitude and the underlying water depth. This whole process shapes the wave. In the parameter space (R_μ, R_ρ), slides of large viscosity and low density $(R_\mu \gg 1, R_\rho \gtrsim 1)$ which generate solitary-like waves, approximately deform as rectangles and produce water elevations η^f at the slide front. Conversely, slides of low viscosity and large density $(R_\mu \gtrsim 1, R_\rho \gg 1)$ have fronts deforming approximately as triangles and induce water elevations η^{tp} at the triple point. In both cases, the analytical expression of $\mathrm{Fr}(t)$ as a function of η^f [Eqs. (21) and (22)] or η^{tp} [Eqs. (23) and (24)] depends on the exact expression of the perturbations' velocity. In any case, the wave maximum amplitude is directly related to the maximum value of the Froude number. This is consistent with $\mathrm{Fr}(t)$ being a quantifier of the volume flux per unit depth of water displaced and therefore rising.

Figure 12 summarizes how the wave maximum amplitude depends on the maximum Froude number. For hydraulic jumps and breaking waves, two analytical laws are obtained, one capturing waves of low Froude numbers ($\mathrm{Fr}_{\max} < 1$) as well as the lowermost branch of waves in Fig. 12 [Eq. (27)], and the linear law $\eta^{tp}(t)/H_w = \mathrm{Fr}(t)$ capturing waves of the uppermost branch at large

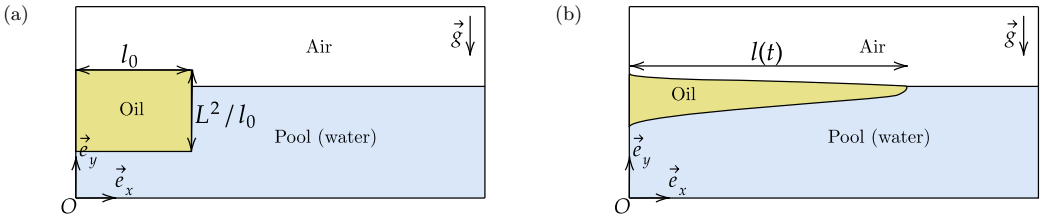

FIG. 14. Representation of the geometry of the problem, (a) initially and (b) at larger times once the oil slick propagates.

Froude numbers ($\mathrm{Fr}_{\max} \geqslant 1$). Unifying equations would require a better modeling of the transient slide deformation during collapse and its connection with the celerity of perturbations.

APPENDIX A: NUMERICAL VALIDATION

Prior to modeling waves generated by a Newtonian collapse, the code was tested quantitatively on a three-phase dam-break flow, modeling the spilling of an oil slick at the interface between air and water (see Fig. 14 for a sketch of the flow). The experimental data used for a comparison were taken from Ref. [37]. Experiments were conducted in a parallelepipedic tank of large width, so the flow is invariant along the width, considered two-dimensional and plane. As detailed in Ref. [37], oil may spread following an inertial regime characterized by the balance of buoyancy and inertia, which yields

$$\frac{l}{L} = \alpha_1 \left(\sqrt{\frac{g\Delta}{L}} t \right)^{2/3}, \tag{A1}$$

with α_1 a coefficient of proportionality, l the length of the oil slick along the direction of spilling, g the acceleration of gravity, L is a length scale whose square is equal to the cross-sectional surface area of the oil slick, t is time, $\Delta = (\rho_w - \rho_{\mathrm{oil}})/\rho_w$ is the density contrast between oil and water, of respective densities ρ_{oil} and ρ_w. Similarly, the oil spill is expected to go through a viscous regime

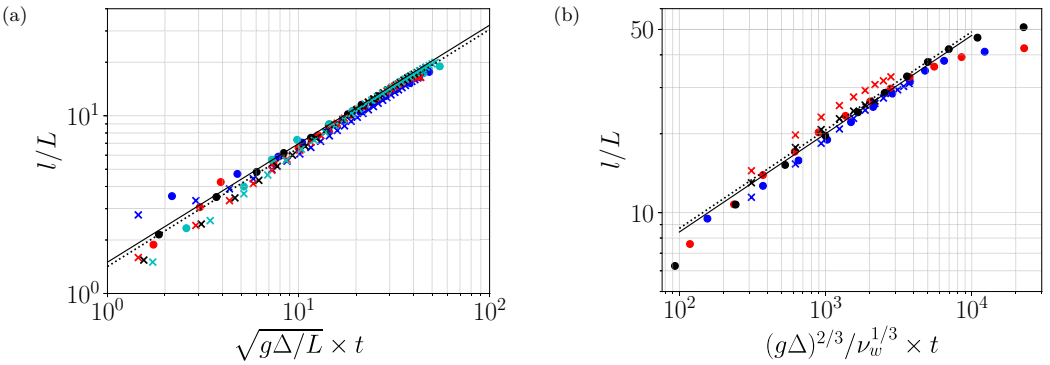

FIG. 15. Test of the numerical methods with experiments from Ref. [37]. Numerical results appear in crosses, experimental data as bullet points. (a) Inertial regime of spilling, with colours corresponding to experiments ● 9, ● 11, ● 14, ● 18 as numbered in Ref. [37], and the regressions — $\alpha_1 = 1.5$ obtained from experiments and ..... $\alpha_1 = 1.42$ obtained from the associated simulations. (b) Viscous regime of spilling, with colors corresponding to experiments ● 19, ● 24, ● 27 as numbered in Ref. [37], and the regressions — $\alpha_2 = 1.5$ from experiments and ..... $\alpha_2 = 1.55$ from simulations.

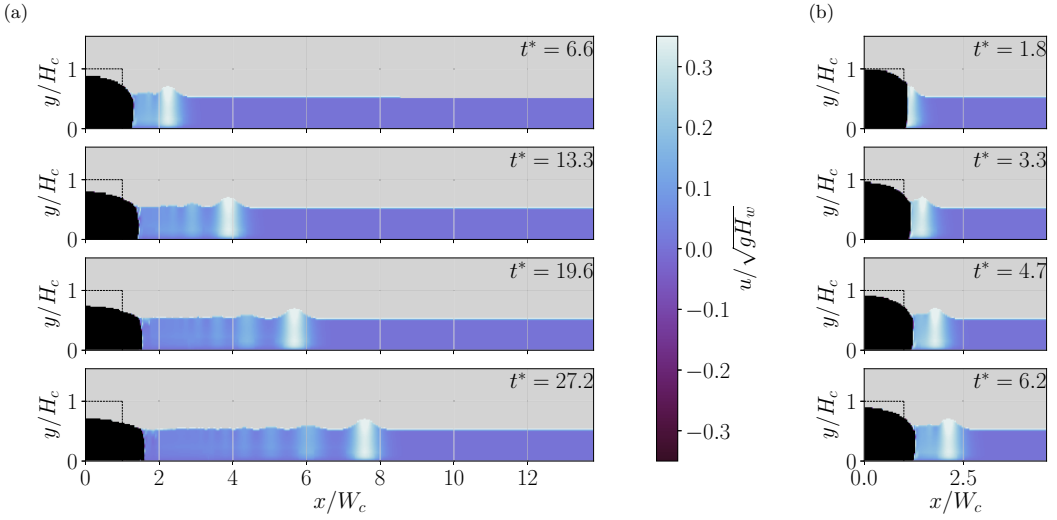

FIG. 16. (a) Solitary-like wave produced from $(R_\mu, R_\rho) = (10^4, 1.2)$. (b) Close-ups near the slide at early times.

characterized by the balance of buoyancy and viscous forces, which yields the law of evolution

$$\frac{l}{L} = \alpha_2 \left[\frac{(g\Delta)^{2/3}}{\nu_w^{1/3}} t \right]^{3/8}, \tag{A2}$$

with α_2 a coefficient of proportionality and ν_w the kinematic viscosity of water.

The previous scalings enable comparison of experimental and numerical data in Figs. 15(a) and 15(b) which evidence different realizations of the oil spill, varying with the initial geometry and size of the parallelepipedic volume of oil. An excellent agreement appears in the inertial regime in Fig. 15(a). Numerical crosses scatter around the dotted line for which $\alpha_1 = 1.42$. This corresponds to a difference of 5.3% compared to the value $\alpha_1 = 1.5$ obtained from experimental bullet points, represented by the solid line. Good agreement is also visible in Fig. 15(b) concerning the viscous

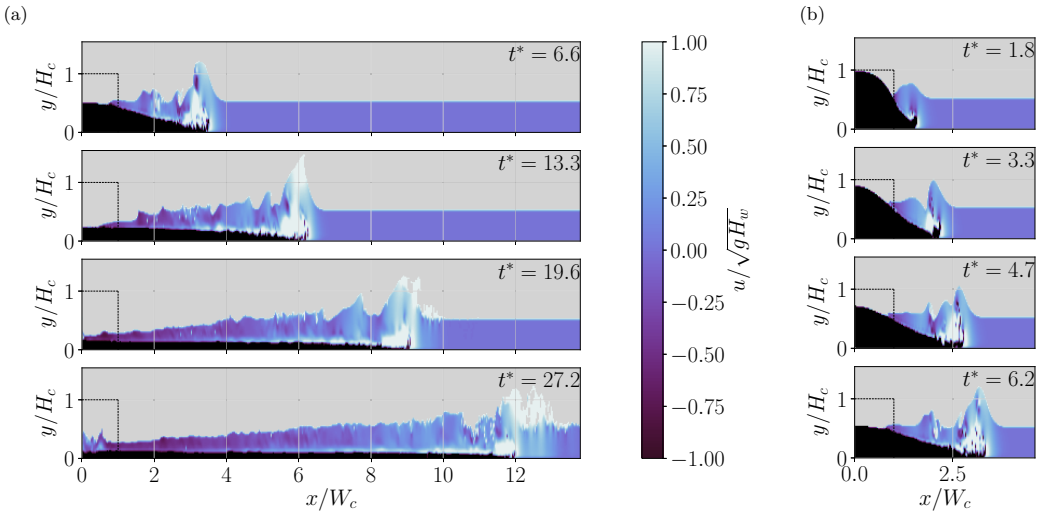

FIG. 17. (a) Roller produced from $(R_\mu, R_\rho) = (1, 14)$. (b) Close-ups near the slide at early times.

TABLE I. Dimensionless numbers corresponding to the experiments of Suchon [37] whose data appear in Fig. 15.

Expt. number	9	11	14	18	19	24	27
Fr	1.48	3.85	2.37	2.40	0.42	1.62	0.721
Re ($\times 10^3$)	73.0	73.0	60.0	43.4	16.6	16.6	9.85

regime. For the three configurations modelled, numerical points evolve with the expected slope 3/8. One simulation slightly exceeds the values of the slick length. It might be due to the low volume of oil initially released, so that the slick may be sensitive to surface tension in experiments, while it is not taken into account in numerical simulations. Experimental bullet points scatter around the model in solid line for which $\alpha_2 = 1.5$ while numerical crosses scatter around a model $\alpha_2 = 1.55$ which is only 3.3% lower. Such agreement confirms the ability of the code to catch the dynamics of spilling which is similar to the one at play during wave formation, and to deal with the presence of three phases at an interface.

Note that in these simulations, the size of the computational domain only differs by 6.7% with respect to simulations of impulse waves. The size of the finest mesh cell is computed in the same way in both cases. Consequently, the sizes of finest cells also differ by 6.7%. Note as well that a Reynolds number can be defined from scale laws as

$$\mathrm{Re} = \frac{\sqrt{g\Delta}L^{3/2}}{\nu_w}, \tag{A3}$$

and, similarly, a Froude number is defined by computing $\dot{l}_{\max}$ from Suchon's experimental values with finite centered differences,

$$\mathrm{Fr} = \frac{\dot{l}_{\max}}{\sqrt{g\Delta L}}. \tag{A4}$$

These dimensionless numbers prove to vary in the same ranges as $\mathrm{Re}_{\max}$ and $\mathrm{Fr}_{\max}$ of the present study or even beyond since Fr = 3.85 largely exceeds the maximum value of $\mathrm{Fr}_{\max}$ around 2 (see

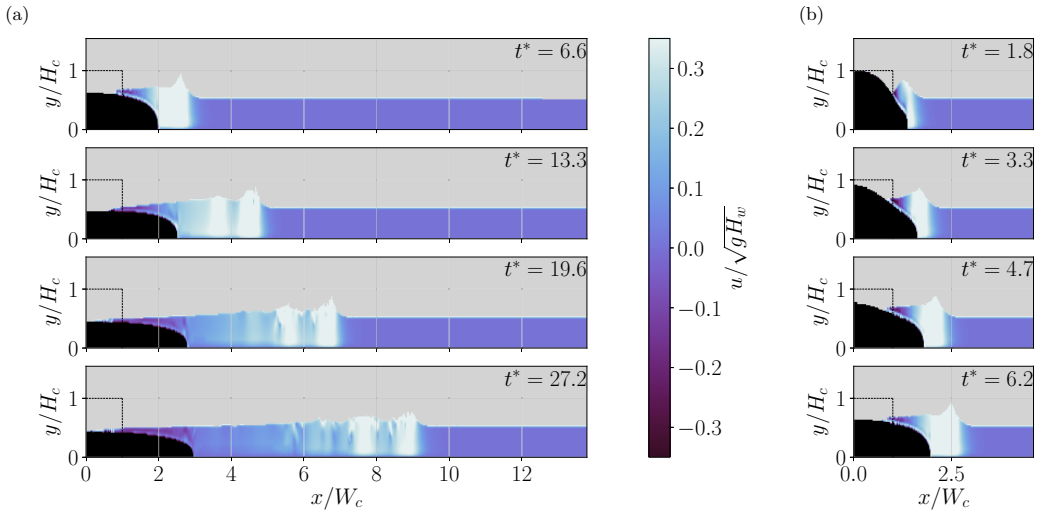

FIG. 18. (a) Hydraulic jump produced from $(R_\mu, R_\rho) = (10^4, 14)$. (b) Close-ups near the slide at early times.

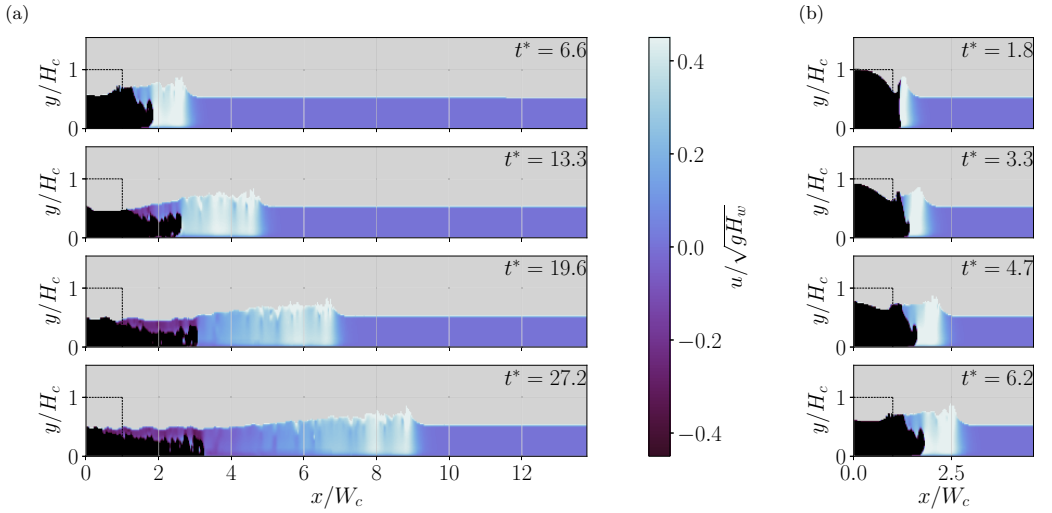

FIG. 19. (a) Hydraulic jump produced from $(R_\mu, R_\rho) = (1, 1.2)$. (b) Close-ups near the slide at early times.

table 1). This further supports the code ability to model wave formation for the region we explore in the parameter space (R_μ, R_ρ).

APPENDIX B: FOUR EXTREMES IN THE PARAMETER SPACE

Further illustrations are gathered in the present Appendix to complement observations on the different types of waves for the four corners of the parameter space (R_μ, R_ρ) – see Figs. 16-19.

[1] M. Ioualalen, J. Asavanant, N. Kaewbanjak, S. T. Grilli, J. T. Kirby, and P. Watts, Modeling the 26 December 2004 Indian Ocean tsunami: Case study of impact in Thailand, J. Geophys. Res.: Oceans **112**(C7) (2007).

[2] H. M. Fritz, F. Mohammed, and J. Yoo, Lituya Bay landslide impact generated mega-tsunami 50th anniversary, in *Tsunami Science Four Years after the 2004 Indian Ocean Tsunami: Part II: Observation and Data Analysis*, edited by P. R. Cummins, K. Satake, and L. S. L. Kong (Birkhäuser, Basel, 2009), pp. 153–175

[3] S. M. Abadie, J. C. Harris, S. T. Grilli, and R. Fabre, Numerical modeling of tsunami waves generated by the flank collapse of the Cumbre Vieja Volcano (La Palma, Canary Islands): Tsunami source and near field effects, J. Geophys. Res.: Oceans **117**(C5) (2012).

[4] K. Kremer, G. Simpson, and S. Girardclos, Giant Lake Geneva tsunami in AD 563, Nat. Geosci. **5**, 756 (2012).

[5] F. Løvholt, S. Glimsdal, P. Lynett, and G. Pedersen, Simulating tsunami propagation in fjords with long-wave models, Nat. Hazards Earth Syst. Sci. **15**, 657 (2015).

[6] J. S. Russel, Report on Waves, Report of the 14th Meeting of the British Association for the Advancement of Science **311–390**, 310 (1844).

[7] J. S. Walder, P. Watts, O. E. Sorensen, and K. Janssen, Tsunamis generated by subaerial mass flows, J. Geophys. Res.: Solid Earth **108** (2003).

[8] P. L.-F. Liu, T.-R. Wu, F. Raichlen, C. E. Synolakis, and J. C. Borrero, Runup and rundown generated by three-dimensional sliding masses, J. Fluid Mech. **536**, 107 (2005).

[9] B. Ataie-Ashtiani and A. Nik-Khah, Impulsive waves caused by subaerial landslides, Environ. Fluid Mech. **8**, 263 (2008).

[10] G. Sælevik, A. Jensen, and G. Pedersen, Experimental investigation of impact generated tsunami; related to a potential rock slide, Western Norway, Coast. Eng. **56**, 897 (2009).
[11] S. Viroulet, D. Cébron, O. Kimmoun, and C. Kharif, Shallow water waves generated by subaerial solid landslides, Geophys. J. Int. **193**, 747 (2013).
[12] V. Heller and W. H. Hager, A universal parameter to predict subaerial landslide tsunamis? J. Mar. Sci. Eng. **2**, 400 (2014).
[13] H. M. Fritz, Ph.D. thesis, Swiss Federal Institute of Technology of Zürich, 2002.
[14] S. Viroulet, A. Sauret, and O. Kimmoun, Tsunami generated by a granular collapse down a rough inclined plane, Europhys. Lett. **105**, 34004 (2014).
[15] S. Viroulet, A. Sauret, O. Kimmoun, and C. Kharif, Granular collapse into water: Toward tsunami landslides, J. Vis. **16**, 189 (2013).
[16] B. Huang, Q. Zhang, J. Wang, C. Luo, X. Chen, and L. Chen, Experimental study on impulse waves generated by gravitational collapse of rectangular granular piles, Phys. Fluids **32**, 033301 (2020).
[17] G. Zitti, C. Ancey, M. Postacchini, and M. Brocchini, Impulse waves generated by snow avalanches: Momentum and energy transfer to a water body, J. Geophys. Res.: Earth Surf. **121**, 2399 (2016).
[18] G. Zitti, C. Ancey, M. Postacchini, and M. Brocchini, Snow avalanches striking water basins: Behaviour of the avalanche's centre of mass and front, Nat. Hazards **88**, 1297 (2017).
[19] V. Heller and W. H. Hager, Impulse product parameter in landslide generated impulse waves, J. Waterw. Port Coast. Ocean Eng. **136**, 145 (2010).
[20] V. Heller and J. Spinneken, Improved landslide-tsunami prediction: Effects of block model parameters and slide model, J. Geophys. Res.: Oceans **118**, 1489 (2013).
[21] F. Mohammed and H. M. Fritz, Physical modeling of tsunamis generated by three-dimensional deformable granular landslides, J. Geophys. Res.: Oceans **117**, C11 (2012).
[22] B. C. McFall and H. M. Fritz, Physical modelling of tsunamis generated by three-dimensional deformable granular landslides on planar and conical island slopes, Proc. R. Soc. A **472**, 20160052 (2016).
[23] M. Robbe-Saule, C. Morize, R. Henaff, Y. Bertho, A. Sauret, and P. Gondret, Experimental investigation of tsunami waves generated by granular collapse into water, J. Fluid Mech. **907**, A11 (2021).
[24] E. Noda, Water waves generated by landslides, J. Waterw. Harb. Coast. Eng. Div. **96**, 835 (1970).
[25] D. G. Goring and F. Raichlen, Propagation of long waves onto shelf, J. Waterw. Port Coast. Ocean Eng. **118**, 43 (1992).
[26] W. Sarlin, C. Morize, A. Sauret, and P. Gondret, Nonlinear regimes of tsunami waves generated by a granular collapse, J. Fluid Mech. **919**, R6 (2021).
[27] S. Popinet and collaborators, Basilisk http://basilisk.fr.
[28] S. Popinet, An accurate adaptive solver for surface-tension-driven interfacial flows, J. Comput. Phys. **228**, 5838 (2009).
[29] J. A. van Hooft, S. Popinet, C. C. van Heerwaarden, S. J. A. van der Linden, S. R. de Roode, and B. J. H. van de Wiel, Towards adaptive grids for atmospheric boundary-layer simulations, Bound.-Layer Meteorol. **167**, 421 (2018).
[30] GDR MiDi, On dense granular flows, Eur. Phys. J. E **14**, 341 (2004).
[31] P. Jop, Y. Forterre, and O. Pouliquen, A constitutive law for dense granular flows, Nature (Lond.) **441**, 727 (2006).
[32] M. Robbe-Saule, C. Morize, Y. Bertho, A. Sauret, and P. Gondret, Experimental study of wave generation by a granular collapse, EPJ Web Conf. **140**, 14007 (2017).
[33] R. L. Miller and R. V. White, *A Single-impulse System for Generating Solitary, Undulating Surge, and Gravity Shock Vaves in the Laboratory*, Technical Report, Fluid Dynamics and Sediment Transport Lab, University of Illinois, Chicago (1966).
[34] A. Ritter, Die fortpflanzung der wasserwellen, Zeitschrift des Vereines Deutscher Ingenieure **36**, 947 (1892).
[35] H. E. Huppert and J. E. Simpson, The slumping of gravity currents, J. Fluid Mech. **99**, 785 (1980).
[36] R. P. Mulligan and W. A. Take, On the transfer of momentum from a granular landslide to a water wave, Coast. Eng. **125**, 16 (2017).
[37] W. Suchon, Master's thesis, Massachusetts Institute of Technology, 1970.